Mesopotamian journal of Big Data
Vol. **(2025)**, 2025, **pp**. 350–368
DOI: https://doi.org/10.58496/MJBD/2025/022 , ISSN: 2958-6453
https://mesopotamian.press/journals/index.php/BigData

Research Article

Optimized Wavelet Scatter Method for Accurate Classification and Segmentation of Lung Nodules

Enas Hamood Al-Saadi[1,*], Ahmed Nidhal Khdiar[2] , Nidhal K. El Abbadi[3]

[1] *Department of Computer, College of Education for Pure Science, University of Babylon, Babylon, Iraq*
[2] *Department of Electrical Engineering, Faculty of Engineering, University of Kufa, Najaf, Iraq*
[3] *Al Mustaqbal Center for AI Applications, Al Mustaqbal University, Babylon, Iraq*

ARTICLEINFO

Article History
Received 27 May-2025
Revised 18 Sep 2025
Accepted 11 Oct 2025
Published 28 Oct 2025

Keywords
Computer-aided diagnosis
Early cancer detection
Feature extraction
Support vector machine
Random forest
Decision tree

ABSTRACT

Lung cancer is a significant global health concern due to its high mortality rate. This is primarily due to the difficulty of identifying malignant growths in early-stage computed tomography (CT) images. The thing is, it's often hard to tell the difference between a benign nodule and a malignant one. This makes it tricky to figure out what's going on with the patient. That's where these computer-aided diagnosis (CAD) approaches come in. This study introduces a lightweight and interpretable framework for comprehensively analyzing lung nodules, including their detection, classification, and segmentation. This approach uses the wavelet scattering transform (WST) to extract stable, deformation-invariant features. These features are then evaluated using three traditional classifiers: The Support Vector Machine (SVM), the Random Forest (RF), and the Decision Tree (DT). The methodology follows a structured pipeline. It begins with image enhancement steps, such as resizing, denoising, and gamma-based contrast optimization. Then, it moves on to WST-based feature representation, classification, and segmentation using Otsu's thresholding technique. Validation experiments were conducted using the SPIE-AAPM Lung CT Challenge dataset in conjunction with the LIDC-IDRI benchmark. This dataset comprises 11,114 annotated CT slices, of which 8,286 are malignant and 2,828 are benign. The results demonstrate the proposed pipeline's effectiveness in delivering accurate and reliable performance. This shows its potential as a supportive tool for early diagnosis and clinical decision-making. Patient-wise separation and stratified 10-fold cross-validation were applied to ensure unbiased evaluation and prevent data leakage. Results show that SVM achieved perfect performance across all metrics (accuracy, precision, recall, and F1-score), while RF and DT yielded 99.33% and 98.18%, respectively. For segmentation, the model reached an Intersection over Union (IoU) of 0.845 and a Dice Similarity Coefficient (DSC) of 0.912. Although the SVM classifier achieved ideal scores, measures such as patient-level grouping, class weighting, and cross-validation were implemented to reduce risks of overfitting. Overall, the integration of WST with classical classifiers provides a lightweight and explainable CAD framework that has strong potential to support early lung cancer detection and clinical decision-making.

1. INTRODUCTION

Lung cancer remains the leading cause of cancer-related mortality worldwide, surpassing deaths from colon, breast, and prostate cancers combined. Recent global statistics report hundreds of thousands of new cases and fatalities annually, emphasizing the urgent necessity for accurate and early diagnosis [1]. Early identification of malignant nodules greatly improves treatment outcomes and survival rates. Nevertheless, manual interpretation of computed tomography (CT) scans is challenging, time-consuming, and subject to observer variability, which highlights the value of computer-aided diagnosis (CAD) systems that support radiologists in detecting and characterizing lung nodules with high accuracy [2].

Despite advancements in medical imaging and artificial intelligence, several barriers still hinder effective lung cancer diagnosis. The challenge of distinguishing malignant lung nodules from their benign counterparts remains formidable, as both categories frequently exhibit analogous visual and structural characteristics, complicating their classification [3]. Well,

*Corresponding author. Email: pure.anas.ehmod@uobabylon.edu.iq

patient-level variations in nodule morphology, density, and size make it tough to make consistent diagnoses. Earlier CAD approaches that relied on handcrafted descriptors were typically limited in their robustness and ability to generalize across datasets. Conversely, although deep learning-based systems offer robust predictive capabilities, they typically necessitate significant computational resources and extensive, labeled data, which may not always be readily available in clinical settings [4].

This situation underscores the ongoing need for diagnostic tools that balance interpretability with computational efficiency. In this context, alternative classical methods have been examined. These include support vector machines (SVM), random forests (RF), and wavelet-driven models. While these approaches are more computationally efficient and transparent than deep neural networks, they may still degrade in accuracy when exposed to noisy data, heterogeneous image properties, or nodules with highly similar appearances [5].

More recently (2021–2024), scientists have presented state-of-the-art approaches, including transformer-based frameworks [6], altered region-expanding methods [7], and composite structures that blend wavelet scattering with deep learning frameworks [8]. While promising, these strategies continue to struggle to balance high accuracy, model interpretability, and computational feasibility. This underscores the importance of mathematically sound, resource-efficient methods that can produce consistent features and dependable classification results without requiring extensive training sets.

To address this gap, the present study develops a comprehensive CAD pipeline for lung nodule assessment. The proposed method uses the Wavelet Scattering Transform (WST) to create deformation-free and consistent representations. These representations are then sorted into groups using three models: Decision Tree (DT), Random Forest (RF), and Support Vector Machine (SVM). The Otsu thresholding method is used to segment malignant nodules for localization, and standardization of CT images is achieved through preprocessing operations such as denoising, resizing, and gamma-based contrast adjustment.

The research has three main goals. (i) Design a robust pipeline. Cover preprocessing, feature extraction, classification, and segmentation of lung nodules. (ii) Compare the effectiveness of DT, RF, and SVM classifiers. (iii) Validate the framework. Use the SPIE–AAPM Lung CT Challenge subset of the LIDC–IDRI dataset. Use widely accepted performance metrics.

The study combines WST with traditional classifiers. This combination delivers a reproducible and computationally efficient CAD framework. The framework is capable of supporting accurate and early lung cancer detection.. It has the potential to enhance diagnostic reliability while minimizing computational costs. Furthermore, it paves the way for future work involving validation across external datasets, adaptive preprocessing methods, and extensions to three-dimensional nodule analysis.

The rest of the paper is organized as follows: Section 2 presents the literature review, Section 3 explains wavelet scattering, Section 4 describes the classification models, Section 5 covers evaluation metrics, Section 6 outlines the proposed methodology, Section 7 discusses experimental results, and Section 8 concludes with recommendations for future work.

2.LITERATURE REVIEW

Despite substantial progress in lung nodule classification and segmentation, critical challenges remain unsolved, especially regarding robustness, generalizability, and computational efficiency. Several recent studies have introduced advanced deep learning-based frameworks, yet many of these systems rely on high computational power, large annotated datasets, or complex model architectures that may limit clinical applicability. Moreover, few studies explore interpretable, mathematically grounded methods that ensure reproducibility while maintaining diagnostic accuracy. This section reviews relevant works and identifies the research gap addressed in this study.

Tianjiao et al. [9] introduced MCAT-Net, a deep segmentation model that uses a separation module for multi-threshold features and a coordinate attention mechanism to better preserve texture and spatial features in CT images. The integration of a Transformer architecture improved long-range dependency modeling. Evaluated on the LIDC-IDRI dataset, MCAT-Net obtained an 88.29% Dice Similarity Coefficient (DSC) and sensitivity of 86.33%, demonstrating significant promise for early diagnosis.

Feng and Jiang [10] proposed a hybrid model combining Dual Path Network (DPN) and Mask R-CNN for segmenting lung nodules from CT scans. While the method achieved a classification accuracy of 97.94%, the authors acknowledged the limitation of a small sample size and emphasized the need for larger datasets to confirm generalizability.

Zheng et al. [11] developed a two-phase detection system for lung nodules: multi-planar nodule identification using U-Net++ and false-positive reduction using dense convolutional networks. The model reached 94.6% sensitivity for small nodules but struggled to recognize very small structures, highlighting a common limitation in deep learning models with multiscale input.

Soltani-Nabipour et al. [12] presented an Improved Region Growing (IRG) algorithm that enhanced classical segmentation by introducing automatic threshold detection, iterative region growth, and edge correction. While the method reported an overall accuracy of 98%, it improved tumor identification by less than 13%, showing limited performance gain.

Rehman et al. [13] used the JSRT dataset to classify 247 3D images via a CNN-based model. After preprocessing and grayscale conversion, classification was performed. However, the model showed relatively poor results compared to other approaches, with 88% accuracy and the highest loss rate among those evaluated.

From the reviewed studies, a clear research gap emerges. Most existing methods are deep learning-based and require large-scale annotated data, high training costs, and lack interpretability. Additionally, limited attention has been given to wavelet-based mathematical feature extraction methods such as Wavelet Scattering Transform (WST), which offers stability, invariance to deformation, and interpretability. Moreover, the reliance on deep segmentation networks increases computational complexity. This study addresses these limitations by integrating WST with classical machine learning classifiers (SVM, RF, DT) and applying lightweight Otsu-based segmentation, offering a reproducible and efficient alternative suitable for clinical settings.

To facilitate comparison and highlight the strengths and limitations of related works, Table I provides a consolidated summary of key methodologies, datasets, evaluation metrics, and identified limitations from recent studies on lung nodule classification and segmentation. This comparative analysis helps to contextualize the novelty and contribution of the proposed approach within the existing body of research.

TABLE I. SUMMARY OF PREVIOUS STUDIES ON LUNG NODULE CLASSIFICATION AND SEGMENTATION

Author	Year	Technique	Dataset	Accuracy / Metrics	Key Limitations
Tianjiao et al. [9]	2024	MCAT-Net + Transformer + Coord. Attention	LIDC-IDRI	DSC: 88.29%, Sens: 86.33%	High complexity, transformer dependency
Feng and Jiang [10]	2022	DPN + Mask R-CNN	Private dataset	Accuracy: ~97.94%	Small sample size, no external validation
Zheng et al. [11]	2021	U-Net++ + Multiscale Dense CNN	LIDC-IDRI	Sensitivity: 94.6%	Limited performance on small nodules
Soltani-Nabipour et al. [12]	2020	Improved Region Growing	LIDC-IDRI	Accuracy: ~98%	Modest improvement, dependent on threshold tuning
Rehman et al. [13]	2020	CNN-based classification	JSRT	Accuracy: 88%	Highest loss rate, weak generalization

3. WAVELET SCATTERING

Wavelet scattering is a way to analyze signals and images using math. It creates feature descriptors that are stable and do not change when translated. This makes it very good for tasks that involve classification. A principal benefit of this approach is its capacity to withstand slight geometric variations while maintaining its discriminatory attributes, a characteristic that distinguishes it from conventional feature extraction techniques. The process involves applying successive layers of wavelet convolutions, combined with nonlinear modulus and averaging steps. This allows for the preservation of high-frequency information, which is often diminished in standard wavelet decomposition. Convolutional neural networks (CNNs) learn filters directly from data. Wavelet scattering uses predefined mathematical filters. These filters generate features that capture textures and edge patterns at multiple scales. They also capture these patterns across spatial and frequency domains. This increases robustness to variability. Although scattering networks and CNNs share a hierarchical structure, their principles differ: scattering relies on mathematically defined wavelet filters, while CNNs learn filters directly from data through convolution, pooling, and subsampling. While CNNs are effective in capturing contextual information, they often struggle to separate fine boundary details from global image characteristics [14].

3.1 Structure of Wavelet Scattering Networks

The wavelet scattering transform is considered one of the most powerful mathematical methods for extracting and analyzing image features. It effectively preserves both spatial and frequency information, which makes it highly suitable

it highly suitable for applications such as texture classification. The general decomposition procedure is illustrated in Fig. 1 [15].

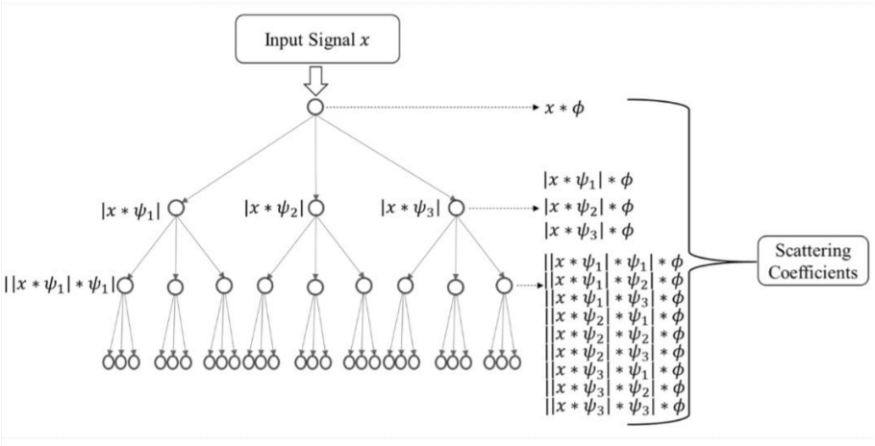

Fig.1. Wavelet Scattering Network [15].

As shown in the figure, wavelet scattering can be understood as a structured network similar in design to convolutional neural networks, but specifically tailored for signal characterization and feature extraction. It is particularly robust against variations and small deformations in the input. The process can be described in the following steps:

1. **Input Signal (x):** The analysis begins with an input signal, denoted as *x*, which represents the data to be processed.
2. **First Convolution Layer:** The signal is convolved with a family of wavelets (ψ_1, ψ_2, ψ_3), generating responses that capture information at different frequencies. The modulus of each response, such as $|x * \psi_1|$, $|x * \psi_2|$, and $|x * \psi_3|$, is then computed [16].
3. **Second Convolution Layer:** The outputs from the first stage are again convolved with the same wavelets to build hierarchical features. This stage is predicated on the modeling of interactions between frequency components. To illustrate, the expression $|x*\psi_1|*\psi_2$ demonstrates the manner in which a second convolution is applied to the response engendered at the first level.
4. **Low-Pass Filtering (Φ):** In this step, both the original input and the higher-order convolutional outputs are processed. They are convoluted with a scaling function ($x*\varphi$). They are processed using a low-pass filter, represented by Φ. This operation stabilizes and smooths the resulting coefficients. It retains meaningful information while reducing sensitivity to noise [17].
5. **Scattering Coefficients:** The result of the procedure is a set of descriptors known as "scattering coefficients." These coefficients form a concise representation. It is informative. It remains robust to minor translations and geometric distortions. This ensures that the extracted features are stable. They are also useful for downstream classification and analysis tasks [18].

4.CLASSIFICATION ALGORITHMS

4.1 Support Vector Machine (SVM)

SVM is a strong and commonly used algorithm in machine learning, especially for tasks where the data is either binary or of two possible values. SVM can separate both linear and nonlinear data by constructing an optimal hyperplane that maximizes the margin between classes. The achievement of this objective by SVM involves the employment of kernel functions that project the input data into a higher-dimensional feature space, thereby enabling the establishment of a linear boundary. This ability makes SVM very good at dealing with complex, non-linear classification challenges [19]. Due to its formidable capacity for generalization and its efficacy in high-dimensional contexts, SVM has emerged as one of the most widely employed methods across a myriad of classification applications in machine learning. It is especially helpful for tasks involving large feature sets since it can accurately establish class boundaries while maintaining computational tractability.

Since $x_i \in R^d$ is the extracted feature vector from the lung CT image and $y_i \in \{-1,+1\}$ is the class label (benign or malignant), the SVM primal optimization problem may be expressed as follows given a training dataset $\{(x_i, y_i)\}_{i=1}^{N}$

$$\min_{w.b.\xi} \frac{1}{2}\|w\|^2 + C\sum_{i=1}^{N}\xi_i \quad (1)$$

Due to:

$$y_i(w.\phi(x_i)+b) \geq 1-\xi_i \quad , \xi_i \geq 0 \quad (2)$$

Here, the weight vector is denoted by w, the bias term by b, the slack variables that permit soft-margin classification by ξ_i, and the regularization constant C regulates the trade-off between margin maximization and classification error minimization. A kernel function implicitly defines the mapping $\phi(\cdot)$. The Radial Basis Function (RBF) kernel was used in this study:

$$K(x_i.x_j) = \exp\left(-\gamma\|x_i - x_j\|^2\right) \quad (3)$$

where each training sample's effect is controlled by γ. With ten-fold cross-validation, grid search was used to optimize both C and γ. SVMs work very well in spaces with several dimensions, such as those generated by wavelet scattering transforms, and have been successfully applied in medical imaging for tumor classification, lesion detection, and disease diagnosis in CT, MRI, and histopathology data. Support vectors define the decision boundary, while the kernel ensures linear separability in the transformed space.

4.2 Decision Tree (DT)

A decision tree shows a sequence of actions and possible outcomes through branching. Its structures resemble trees, where each branch represents a rule of decision and every node represents a feature. They can handle both numerical and category data and are intuitive. Large dataset classifications can be made accurately and quickly with DT [20].

Binary splits are used to recursively divide the feature space into smaller sections in the (DT), a non-parametric classification model that eventually produces class predictions at the leaf nodes. The method chooses the feature and threshold at each node based on a splitting criterion that produce the greatest purity improvement. In this work, the Gini Impurity was used:

$$Gini(t) = 1 - \sum_{k=1}^{K} p_k^2 \quad (4)$$

Where the percentage of samples in class k at node t is denoted by p_k. An alternative impurity measure is entropy, given by:

$$Entropy(t) = -\sum_{k=1}^{K} p_k log_2 p_k \quad (5)$$

with Information Gain calculated as the reduction in entropy after a split.

In this work, the maximum depth was tuned via grid search to control overfitting, the splitting criterion was set to Gini impurity, and the minimum samples per split were set to 2.

4.3 Random Forest (RF)

One popular and significant ensemble-supervised classification algorithm is Random Forest. RF's high accuracy, durability, and ability to provide insights by ranking its features have made it an effective tool for different machine-learning applications, such as medical images. Each decision tree in RF is created by the bagging algorithm without pruning, creating a "Forest" of classifiers that vote for particular classifications [21].

An ensemble technique called the (RF) algorithm aggregates the results of several decision trees to decrease overfitting and increase prediction accuracy. At each split, a random subset of features is chosen, and each tree is trained using a distinct bootstrap sample of the training data. A majority vote is used to determine the final prediction for each tree:

$$\hat{y} = mod\{(h_b(x))\}_{b=1}^{B} \quad (6)$$

where B represents the total number of trees in the forest and $h_b(x)$ represents the prediction produced by the decision tree with index b. In this work, the number of trees (B) was set to 100, and the maximum features per split $\sqrt{d}$ (where d is the number of features)

and Splitting criterion is Gini impurity

5. PERFORMANCE EVALUATION

Using common evaluation criteria, such as Accuracy, Recall (Sensitivity), Precision, and F1-Score, which were all obtained from the confusion matrix of predicted versus real class labels, the performance of the suggested classification framework was quantitatively evaluated. Together, these measures offer a strong assessment of the model's clinical usefulness and offer contrasting viewpoints on its behavior. The percentage of correctly categorized examples among all examined cases is known as accuracy, and it is defined as follows:

$$Acc = \frac{(TP+TN)}{(TP+TN+FP+FN} \quad (7)$$

Whereas FP (False Positives) are benign nodules that are mistakenly classified as malignant, FN (False Negatives) are malignant nodules that are mistakenly classified as benign, and TP (True Positives) are malignant nodules that are correctly classified as malignant.

Precision measures the percentage of malignant nodules that are accurately diagnosed out of all nodules that were anticipated to be malignant. It is calculated as follows:

$$Pre = \frac{TP}{(TP+FP)} \quad (8)$$

A model with high precision generates fewer false alarms, which is essential for minimizing needless follow-up scans and invasive diagnostic treatments for patients.

Recall, sometimes referred to as Sensitivity or True Positive Rate, quantifies how well the model can identify cancerous nodules and is written as follows:

$$Rec = \frac{TP}{(TP+FN)} \quad (9)$$

In medical diagnosis, high recall is particularly important because false negatives (missed malignant nodules) can have severe consequences for patient outcomes.

In order to balance the trade-off between precision and recall and provide a single statistic that takes into account both false positives and false negatives, the F1-Score is the harmonic mean of the two:

$$\text{F1-Score} = 2 \times \frac{\text{Pre}\times\text{Rec}}{\text{Pre}+\text{Rec}} \quad (10)$$

A model with a high F1-Score is one that only identifies malignant nodules accurately but also minimizes missed diagnoses, making it a strong indicator of robustness in imbalanced clinical datasets.

6. PROPOSED METHOD

The aim of this proposal is the detection, classification, and localization of nodules in CT scans of the lung. In this paper, the LIDC-IDRI dataset's SPIE-AAPM Lung CT Challenge subset was utilized which consists of 11,114 annotated 2D CT slices representing 8,286 malignant and 2,828 benign nodules [10]. Each nodule was reviewed by up to four radiologists. For malignancy labels, we adopted the consensus label where available or used a majority vote approach. Importantly, to prevent data correlation and leakage, we ensured that slices from the same patient were not shared across training and test sets. This was achieved by grouping images at the patient level, and then performing 10-fold stratified cross-validation, maintaining class balance within each fold. We do not combine 80/20 split with 10-fold cross-validation; instead, the reference to “80/20” pertains to the proportion of folds used for training (8 folds) and testing (2 folds) within each cross-validation iteration. To address class imbalance, class weighting was applied during classifier training to prevent

bias toward the majority (malignant) class. This methodology ensures a fair, leakage-free, and balanced evaluation of the proposed system. A sample of dataset images is presented in Fig. 2.

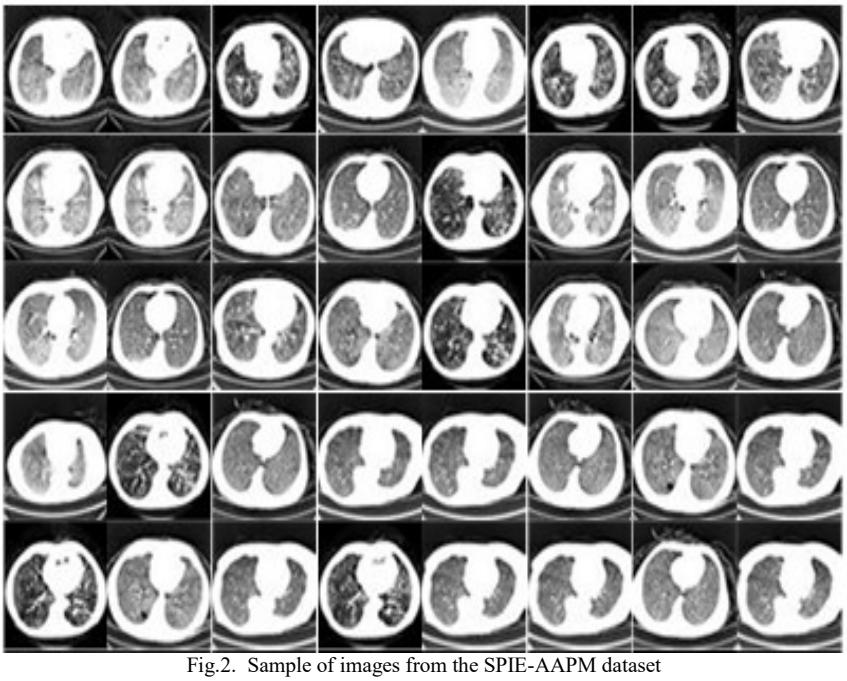

Fig.2. Sample of images from the SPIE-AAPM dataset

Using this dataset, the suggested model's architecture was created, as shown in Fig. 3.

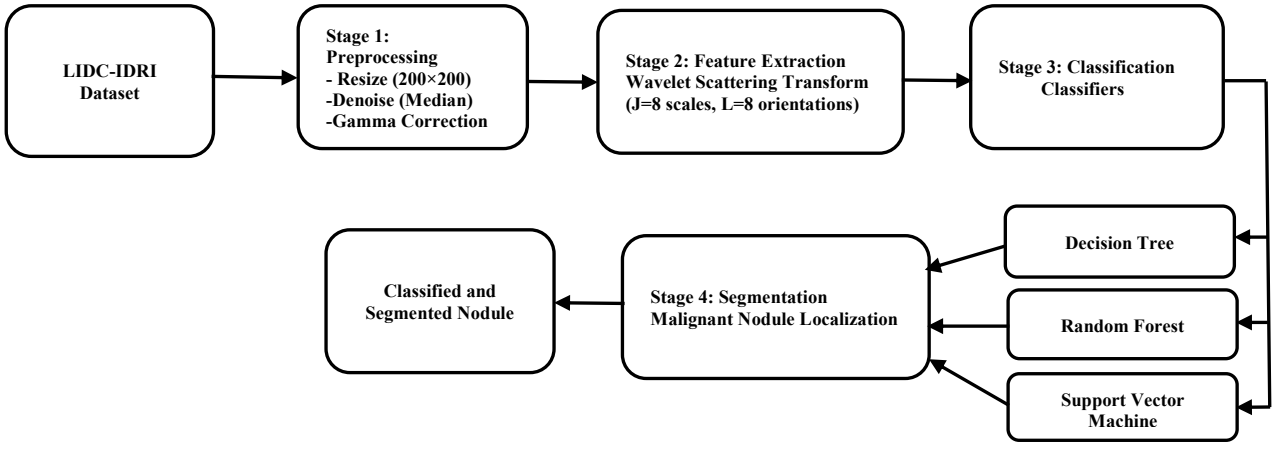

Fig.3.The suggested. model architecture

The training phase block diagram for the stages of the suggested strategy is displayed in Fig. 4, while the test phase block diagram is shown in Fig. 5. To achieve the aim of this proposal, the network was trained on both benign and malignant lung images, and then the trained network was tested with different images.

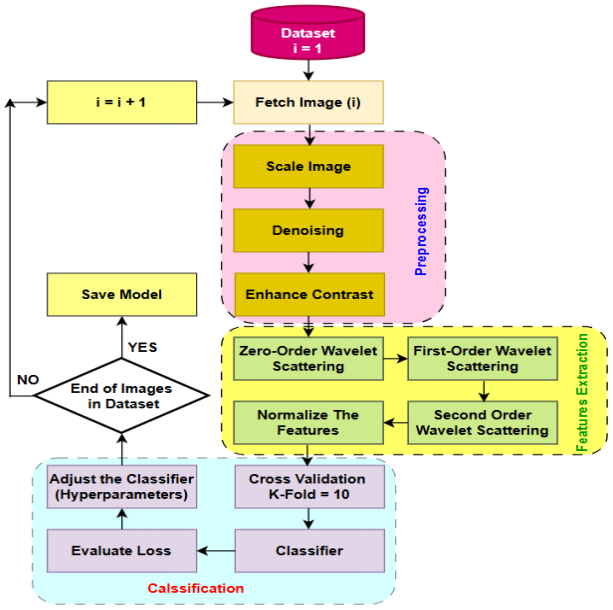

Fig. 4. Training phase block diagram.

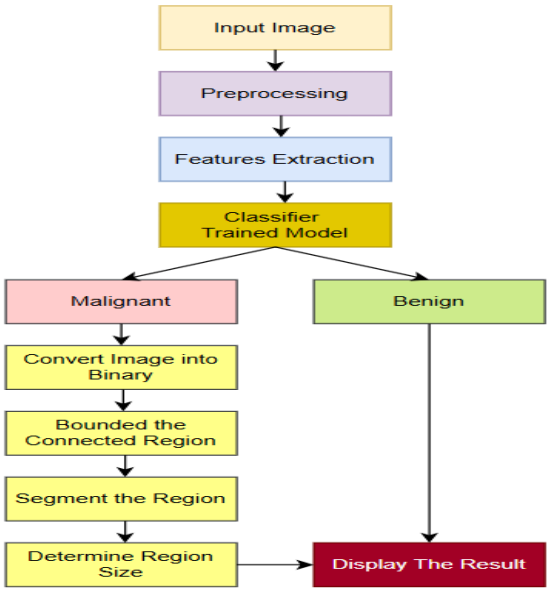

Fig. 5. Testing phase block diagram.

Stage 1: Preprocessing Stage

The input image to the model, whether for training or testing, is enhanced to be suitable for further processing. This is achieved during the preprocessing stage, which includes three steps.

Image Resize: The first preprocessing step involves resizing the images to a fixed size of 200×200 pixels to ensure consistency for analysis. CT and X-ray lung scans often differ in resolution; they also differ in image size. This can create inconsistencies when you apply them to computational models or machine learning pipelines. This issue was addressed by normalizing all images to a uniform dimension to ensure consistent batch processing and reduce computational cost. In the present study, image resizing was executed through the implementation of bicubic interpolation. Each pixel is determined by this method through the combination of weighted contributions from sixteen nearby pixels. Smoother results and more effective preservation of structural information are produced by this method compared to basic interpolation techniques. Maintaining essential details meant standardizing all images to 200×200 pixels. This allowed for more stable and consistent performance of subsequent processes, such as feature extraction and classification.

Noise Removal (Denoising): Random noise often degrades lung images, obscuring anatomical details. One common type of artifact is salt-and-pepper noise, which appears as scattered black and white pixels. This type of noise is caused by sensor limitations or transmission errors. To address this issue, a median filter with a 3×3 sliding window was applied. Each central pixel is replaced with the median of its neighborhood, and impulsive noise is effectively suppressed while edge sharpness is maintained. It is especially important to preserve this information in medical imaging because blurred boundaries can make it difficult to detect nodules and increase the risk of misclassification.

Contrast Enhancement: The final preprocessing step involved enhancing the image's contrast using gamma correction. Many CT images suffer from low contrast, which makes differentiating nodules or lesions challenging. Gamma correction adjusts pixel intensities through a nonlinear transformation, raising them to a power defined by the gamma parameter. Selecting an appropriate gamma value is crucial: overly high values may cause nodules to blend with the background, while low values may exaggerate irrelevant structures. In this study, different gamma settings were tested, and the optimal value was chosen based on its ability to improve clarity and highlight diagnostically significant features. Applying the optimal gamma correction increases the contrast between tissues and highlights edges, helping subsequent processes like segmentation and classification to perform more accurately.

Stage 2: Feature Extraction Using Wavelet Scattering

Wavelet scattering is a mathematical method for feature extraction and signal processing. It breaks down a signal into wavelets defined by a specific frequency and time domain. In this method, the number of layers (L) used is (8) layers. The decomposition process is typically performed using a filter bank with a low-pass and high-pass filter. The low-pass filter

is used to separate the signal's low-frequency components, whereas the signal's high-frequency components are extracted using a high-pass filter. The scaling factor (J) is used to determine the level of signal analysis. (J) represents the number of times the wavelet transform is applied and increases with the desired level of detail obtained; in this proposal, (J) = 8. The wavelet coefficients represent the signal's frequency and time domain characteristics at different scales (refers to the frequency range that a particular wavelet coefficient represents). These coefficients can be analyzed to extract useful features from the signal.

In this stage, invariant features are extracted at multiple levels of abstraction. The wavelet scatter used in this proposal applied eight scales to the image (decomposing the image to eight levels).

We also used eight orientations to capture images directionally, which helped to extract texture and structural information from different directions. Different structural information can be achieved by breaking the image data into three orders.

Wavelet filtering was not applied, and the zero order scattering served as a baseline. In this step, the overall structure of the image is maintained while the global low-frequency content is captured. The first order scattering was composed of various orientations and scales. The feature's capacity to depict image structure is improved by its ability to capture finer features at various scales, including edge and texture. Higher-order correlations between image components at various scales and orientations are detected by the second order scattering, which also captures the image's more complex patterns and interactions. Scattering coefficients are retrieved and normalized to prevent skewness in the feature collection. Repetitive coefficients must be managed in order to avoid bias and lessen the over-representation of particular traits. To facilitate the advanced image analysis and classification, a features vector is created by combining the results for first-, second-, and zero order scattering coefficients.

Algorithm 1 outlines the procedures of wavelet scattering used in the proposal method for feature extraction.

Algorithm 1: Extracting Features from Wavelet Scattering

Input: Digital Image

Output: A normalized vector of features

Step 1: Configuration of Wavelet Scattering

a. Set the scale parameter to 7 (i.e., 8 levels of decomposition).

b. For each scale **s** ∈ {1, 2, ..., 8}:

i. Directed details can be extracted by applying the wavelet transform with 8 orientations.

Step 2: Zero Order Scattering

a. Extract the image's global low frequency information.

b. At this stage, wavelet filtering is not used.

Step 3: First Order Scattering

a. With regard to every scale and orientation:

i. Use the wavelet transform to record textures and edges at various sizes.

ii. The generated first order scattering coefficients should be stored.

Step 4: Second Order Scattering

a. Regarding every scale and also orientation:

i. On the first order coefficients, apply the wavelet transform.

ii. On different scales, extract the higher order correlations of the features.

iii. The second order scattering coefficients that result should be stored.

Step 5: Feature Set Formation

a. Concatenate the scattering coefficients of the first, second, and zero orders.

b. Form a unified feature vector from the concatenated coefficients.

Step 6: Normalization and Redundancy Handling

a. Normalize all scattering coefficients to a common scale.

b. Address redundant or edge-related coefficients to minimize their influence on the feature vector.

Step 7: Output

Return the final normalized feature vector for downstream analysis or classification.

In this stage, the Wavelet Scattering Transform (WST) was used to extract robust, translation-invariant, and deformation-stable features from lung CT images. WST applies a cascade of complex Morlet wavelets across multiple scales and orientations, followed by modulus nonlinearity and low-pass averaging, producing scattering coefficients that retain high-frequency textural information while remaining insensitive to small geometric deformations. Each image was decomposed using J=8 dyadic scales and L=8 orientations per scale, capturing structural details from coarse to fine resolutions across multiple directions. The decomposition consists of three orders: zero-order scattering S_0 representing global low-frequency content, first-order scattering S_1 capturing localized edges and textures, and second-order scattering S_2 modeling higher-order interactions across scales and orientations. Mathematically, the scattering coefficients are computed a:

$$S_0 x = x * \phi_J \quad (11)$$

$$S_1 x = |x * \psi_{\lambda 1}| * \phi_J \quad (12)$$

$$S_2 x = \big||x * \psi_{\lambda 1}| * \psi_{\lambda 2}\big| \quad (13)$$

Here, ψ_λ denotes a complex wavelet at scale–orientation index $\lambda=(J,\theta)$ and ϕ_J is the low-pass filter at scale J. This configuration produces a total of $1+J\times L+J\times L^2$ scattering paths across the three orders. All coefficients are concatenated into a single feature vector and standardized via z-score normalization, which centers each feature at its mean and scales it by its standard deviation, ensuring intensity invariance and facilitating classifier convergence. After discarding redundant and edge-related coefficients, the final representation contains roughly 2,048 dimensions per image, yielding a compact yet information-rich descriptor for classification using SVM, RF, and DT models.

Stage 3: Classification Stage

The classification stage, which is the third step, uses the chosen classifier to categorize the feature set that was taken from the wavelet scattering stage as either malignant or benign.

In this proposal, we choose three types of classifiers: SVM, RF, and DT to select the best classifier that can combine with wavelet scatter to produce the best accuracy.

This method divides the dataset into ten equal sections, called folds, and evaluates the accuracy each fold provides. For practical purposes in lung nodule classification, The model that is most accurate is selected as the good generalization model.

Stage 4: Nodules Segmentation

After classifying the nodule as malignant, the malignant nodule must be segmented, this process means localizing the nodule which helps the physicians to know exactly the location of the nodule.

First, the gray image is transformed into a binary image based on the threshold. The threshold is determined by using the Otsu method (Minimal variation between segments).

The smallest connected white pixel region in the binary image is identified as the nodule, so the color of every pixel outside this region is converted into black color when the nodule(s) are isolated, then can be measured in their center and area.

The final step in the segmentation stage is to measure the nodule's size and dimensions. The area of the nodule is represented by how many white pixels there are in the finished image. Also, the center of the nodule in the image must be determined.

As outlined in Algorithm 2, an automated segmentation method is applied to accurately localize and measure malignant nodules.

Algorithm 2: Segmentation of Malignant Nodules
Input: CT image in grayscale previously classified as malignant
Output: Binary mask of the segmented nodule, its centroid coordinates, total area, and equivalent diameter
Step 1: Otsu-Based Thresholding **a.** Derive the intensity histogram of the input image. **b.** For every possible threshold T, calculate the within-class variance: $\sigma_w^2(T) = w_1(T)\sigma_1^2(T) + w_2(T)\sigma_2^2(T)$. where ω_1, ω_2 represent the probabilities of each pixel group, and σ_1^2, σ_2^2 are their respective variances. **c.** Determine the optimal threshold T^* that minimizes σ_w^2 (T). **d.** Convert the image into a binary mask using:

$$B(x.y) = \begin{cases} 1 & (x.y) > T^* \\ 0 & (x.y) < T^* \end{cases}$$

Step 2: Connected Component Analysis

a. Detect all connected white regions in *B(x,y)* using 8-connectivity.

b. Select the region that matches expected nodule properties (size, compactness, and intensity).

Step 3: Morphological Operations

a. Apply an opening operation to suppress small artifacts.

b. Apply a closing operation to fill small gaps and smooth the contour of the segmented nodule.

Step 4: Nodule Property Calculation

a. Find the centroid coordinates:

$x_c = \frac{1}{N}\sum_{i=1}^{N} x_i \ . \ y_c = \frac{1}{N}\sum_{i=1}^{N} y_i$, where *N* is the number of foreground pixels.

b. Compute the area of the nodule by counting all white pixels.

c. Derive the equivalent diameter: $Deq = 2\sqrt{\frac{A}{\pi}}$, Were, A denotes the nodule area, measured as the total number of white pixels within the segmented region.

Step 5: Segmentation Quality Assessment

a. Compare the predicted mask *M(x,y)* with the ground truth mask *G(x,y)*.

b. Evaluate overlap-based measures:

$$DSC = \frac{2|M \cap G|}{|M| + |G|}, \quad IoU = \frac{|M \cap G|}{|M \cup G|}$$

Step 6: Output: Segmented nodule mask with centroid, area, equivalent diameter, and evaluation metrics (*DSC* and *IoU*).

7. RESULTS AND DISCUSSION

The proposed method was tested to identify the optimal settings for the algorithm's parameters to enhance efficiency, assess the network's performance in detection and classification, and evaluate the segmentation process.
To evaluate the proposed model, we aim to present all results that highlight the effectiveness of each step in the model.

7.1 Preprocessing

The two main steps in preprocessing are image denoising and contrast enhancement. Denoising is performed using a median filter, and its effectiveness is illustrated in Fig. 6.

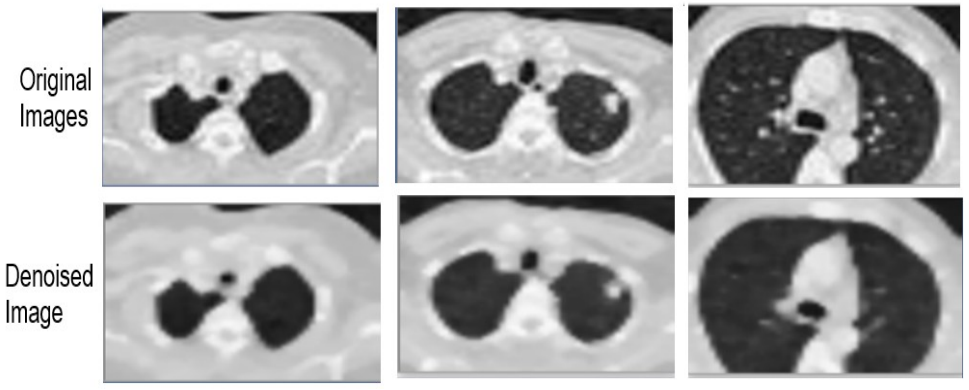

Fig. 6. The denoising of the lung images.

For contrast enhancement, as mentioned in the previous section, the value of gamma has a significant impact on image contrast. To demonstrate this, we applied a high gamma value (such as seven) to the input images, as shown in Fig. 7. In

this case, the nodule becomes nearly indistinguishable from the background, leading to confusion with other regions that are not related to the actual nodule.

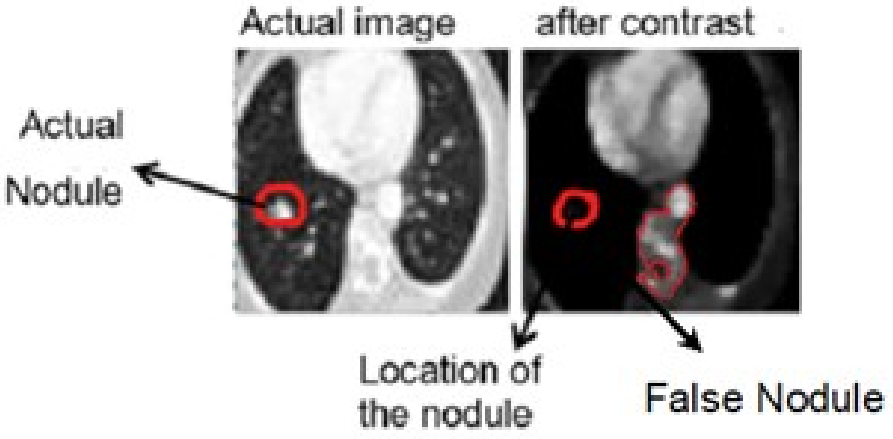

Fig. 7. The results of segmentation when using gamma value equal seven.

Conversely, when a low gamma value is used (in this case, gamma equals 0.1), multiple regions may be misidentified as nodules, making it challenging to recognize the actual nodule, as illustrated in Fig. 8.

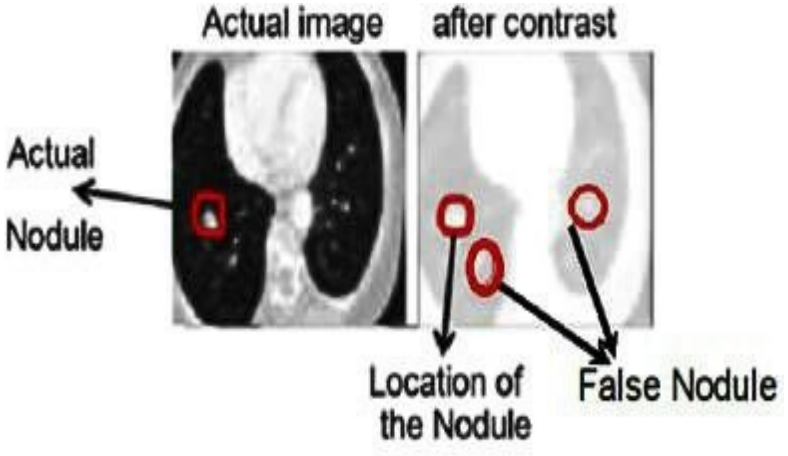

Fig. 8. Using a small gamma value which leads to confusion in nodule identification. .

The gamma value was determined experimentally for this work, and the optimal value for enhancing contrast was found to be 1.2, as shown in Fig. 9.

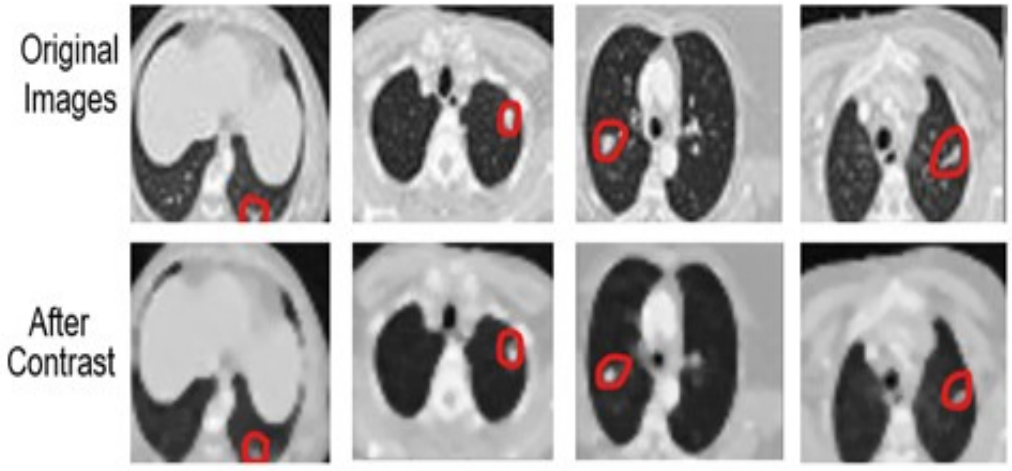

Fig. 9. The results of segmentation when using gamma value equal 1.2.

The gamma value used for contrast enhancement in this study was selected through empirical testing across the SPIE-AAPM dataset. Multiple gamma values were evaluated, and $\gamma = 1.2$ consistently produced optimal visual clarity and segmentation accuracy, making it the preferred choice. This setting effectively balanced the visibility of nodules against background tissues, minimizing both under-enhancement and over-saturation. But this experimentally established fixed value is naturally adjusted to the training dataset's particular intensity characteristics. In real-world applications, CT images often differ significantly in brightness, contrast, and noise levels due to variations in scanning protocols, equipment, and patient anatomy. As such, while $\gamma = 1.2$ is effective within the current scope, it may not generalize well to other datasets or clinical environments. This highlights the need for more flexible contrast enhancement strategies that can adapt to individual image characteristics dynamically. Exploring adaptive methods or machine learning-based contrast adjustment may help improve robustness and ensure consistent performance across broader imaging conditions.

The suggested classification algorithm classified lung images into two categories (benign or malignant). A sample of these images is shown in Fig. 10.

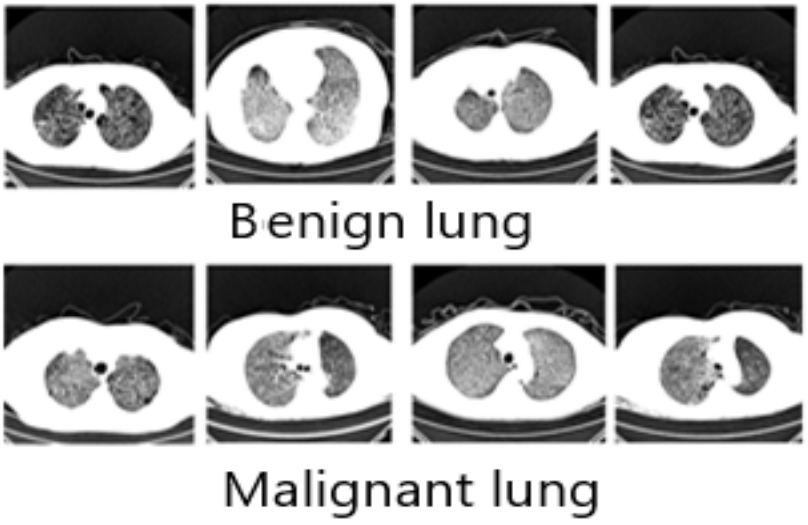

Fig. 10. Sample of benign and malignant images.

7.2 Nodules Segmentation:

In the segmentation step, a binary image is created from the grayscale one based on a threshold calculated by OTSU algorithm. A sample of converted images is shown in Fig. 11.

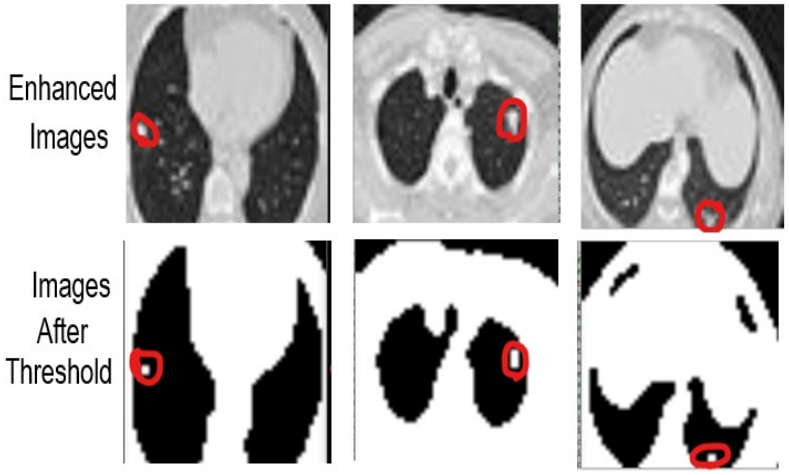

Fig. 11. Converting the grayscale images into binary images.

Then, the smallest connected region (pixels) represents the nodule. This region can be bounded or labeled as a malignant nodule. A sample of this step's results is shown in Fig. 12.

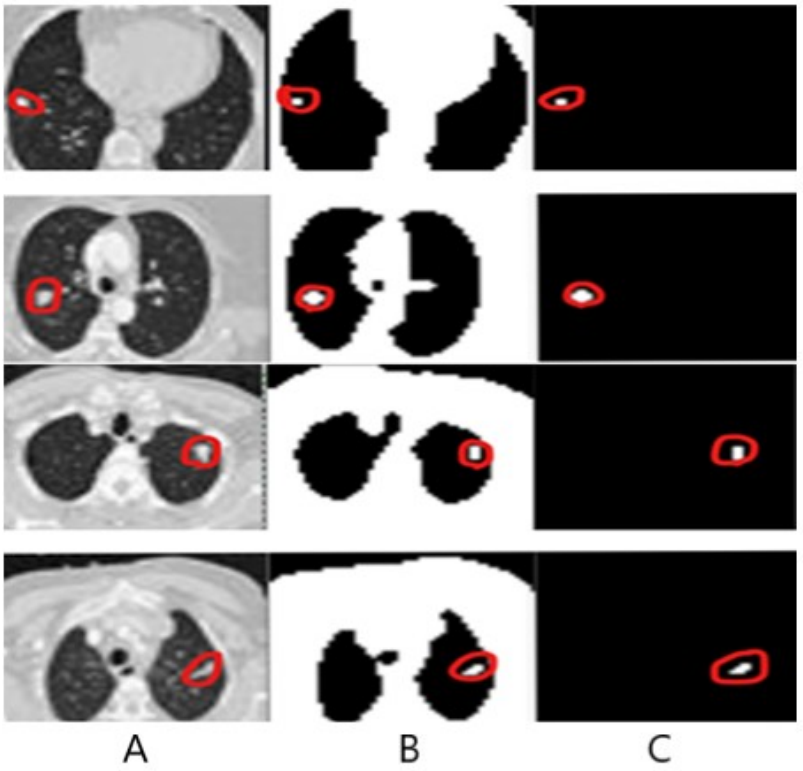

Fig. 12. Steps of isolating the nodule: (A) enhanced image, (B) binary image, (C) segmented nodules.

When the nodule is identified, all the other background regions are converted into black color as shown in Fig. 13.

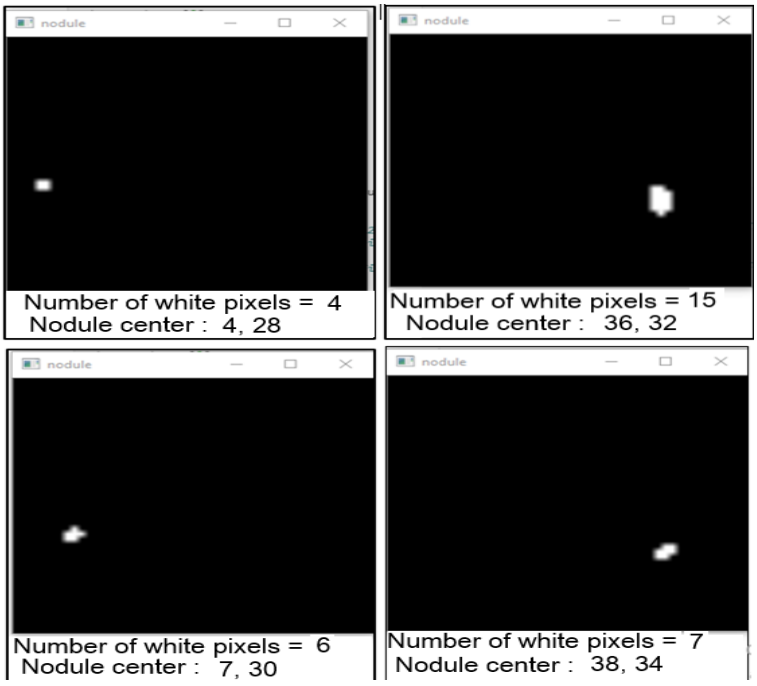

Fig. 13. Sample, measuring the area and location of the segmented nodule.

To objectively assess segmentation accuracy, we computed two standard measures based on overlap: Intersection over Union (IoU) and the Dice Similarity Coefficient (DSC). These metrics compare a predicted binary nodule masks with the ground truth annotations provided in the SPIE-AAPM dataset. Across the 606 test images represent the subset of test images (from across all CV folds) that were classified as malignant and subsequently used in segmentation evaluation, the segmentation module obtained a mean IoU of 0.845 and a mean DSC of 0.912. These results demonstrate that the proposed Otsu-based segmentation approach, when applied after accurate nodule classification, is capable of delineating the spatial extent of malignant nodules with high precision and the reported metrics confirm the model's robustness quantitatively. To contextualize the performance of our segmentation method, Table II compares the suggested method and current state-of-the-art lung nodule segmentation techniques based on standard evaluation metrics, including the IoU and DSC.

TABLE II. COMPARISON OF PROPOSED METHOD WITH RECENT LUNG NODULE SEGMENTATION TECHNIQUES USING DICE AND IOU METRICS

Author	Year	Technique	Dataset	Accuracy / Metrics	Key Limitations
Tianjiao et al. [9]	2024	MCAT-Net + Transformer + Coord. Attention	LIDC-IDRI	DSC: 88.29%, Sens: 86.33%	High complexity, transformer dependency
Feng and Jiang [10]	2022	DPN + Mask R-CNN	Private dataset	Accuracy: ~97.94%	Small sample size, no external validation
Zheng et al. [11]	2021	U-Net++ + Multiscale Dense CNN	LIDC-IDRI	Sensitivity: 94.6%	Limited performance on small nodules
Soltani-Nabipour et al. [12]	2020	Improved Region Growing	LIDC-IDRI	Accuracy: ~98%	Modest improvement, dependent on threshold tuning
Rehman et al. [13]	2020	CNN-based classification	JSRT	Accuracy: 88%	Highest loss rate, weak generalization

Table II shows that the proposed Otsu and Wavelet SVM segmentation method achieves a 0.845 on the IoU and 0.912 on the dice. This performance surpasses MCAT-Net and Multiplanar CNN approaches and closely approaches that of the more complex DPN + Mask-RCNN model. These findings indicate that the proposed lightweight method can deliver high segmentation accuracy with reduced computational demands, demonstrating both its effectiveness and practical potential for clinical applications.

7.3 Evaluate the Model Performance

A collection of lung images was used to train the proposed model, as mentioned previously, using three different classifiers (SVM, RF, and DT). To test the performance of the trained model, we used 606 images: 404 malignant and 202 benign.

To assess the three classifiers' performance, confusion matrices were created. Fig. 14 illustrates the confusion matrices

for SVM, RF, and DT. Performance metrics were calculated from the confusion matrix for each classifier and are summarized in Table III.

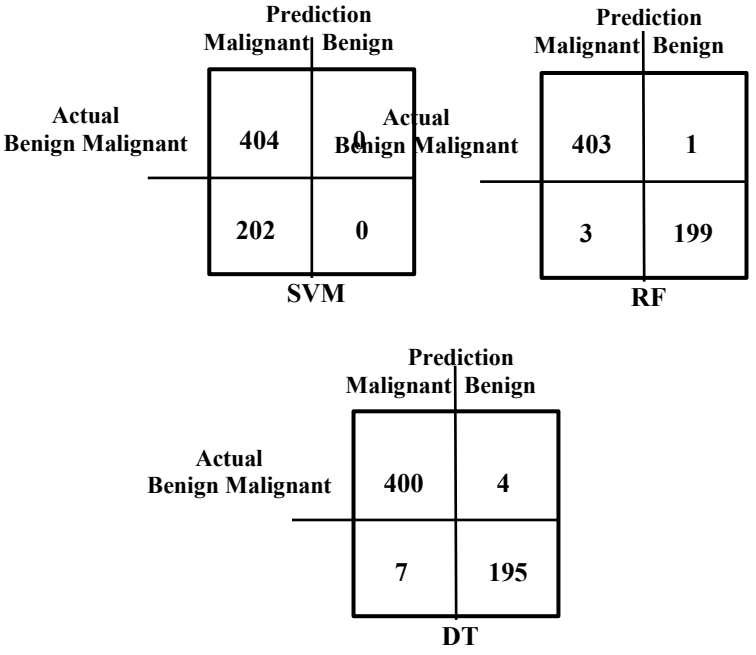

Fig. 14. Confusion matrices for three classifiers.

TABLE III. PERFORMANCE TOOLS FOR THREE CLASSIFIERS.

Tools / Classifier	Accuracy	Precision	Recall	F1-Score
SVM	100	100	100	100
RF	99.33	99.26	99.75	99.50
DT	98.18	98.28	99.00	98.63

The proposed framework demonstrated outstanding performance in classifying all tested images. As shown in Table III, a perfect classification outcome was achieved by the Support Vector Machine (SVM), with 100% being reached in accuracy, precision, recall, and F1-score across the evaluation folds. The Random Forest (RF) and Decision Tree (DT) models also performed well, achieving accuracies of 99.33% and 98.18%, respectively. These results show that SVM is very good at dealing with the complicated, high-dimensional feature space made by the Wavelet Scattering Transform (WST), and it can generalize well and resist overfitting. On the other hand, although DT classifiers are easier to understand, they are more likely to overfit when faced with complicated feature sets.

Achieving 100% accuracy with SVM in medical imaging is an exceptional outcome. Therefore, it is necessary to thoroughly validate it. Several precautions were adopted to ensure the reliability of the evaluation. First, CT slices were grouped by patient to ensure that data from the same subject would not be split between the training and testing sets, thus eliminating potential data leakage. Secondly, stratified 10-fold cross-validation was utilized to maintain class distribution across folds and ensure that each sample was evaluated once. Third, class weighting was applied to mitigate the imbalance between malignant and benign nodules. So, all these steps made sure that the validation process was strong, fair, and didn't have any leaks.

Table IV shows that the proposed framework is better than other methods. It compares how well the framework worked against older methods. The framework worked better than the older methods every time.

Table IV. COMPARING THE SUGGESTED METHOD WITH PREVIOUS METHODS.

Author	Year	Method	Accuracy%
(Q. Song et al., 2017) [22]	2017	CNN	84.2
(S. Hussein et al., 2017) [23]	2017	High-level attributes + CNN	92.3
(A. Nibali et al., 2017) [24]	2017	Rest Net	89.9
(W. Shen et al., 2017) [25]	2017	Convolutional Neural Networks for Multiple Crops	87.14
(S. Hussein et al., 2017) [26]	2017	3D Multi-task Learning Using CNN	91.26
(Y. Xie et al., 2017) [27]	2017	Transferable Multi-Model Ensemble	91
(Y. Xie et al., 2018) [28]	2018	Combining Deep Model-Learned Data, Texture, and Shape at the Decision Level	88.73
(Y. Xie et al., 2019) [29]	2019	Deep learning	91.6
(G. Zhang et al., 2019) [30]	2019	Hybrid features	93.78
(P. Wu et al., 2020) [31]	2020	Deep residual networks and migration learning	98.23
(G. Shah et al., 2020) [32]	2020	Deep learning	95
(E. Lv et al., 2021) [33]	2021	Deep Convolutional Network	96
(G. Zhang et al., 2021) [34]	2021	3D DenseNet	92.4
(J. Feng and J. Jiang, 2022) [10]	2022	Deep Learning	97.94
P. Bruntha et al., 2022) [35]	2022	Transfer learning	97.93
Proposed model	2024	Wavelet scattering and SVM	100

Table IV presents a comparative analysis of the suggested framework and formerly documented techniques for lung nodule categorization. Integrating Wavelet Scattering Transform with Support Vector Machine (SVM) technology achieved 100% accuracy, surpassing deep learning approaches such as Convolutional Neural Networks (CNNs), DenseNet, and hybrid architectures. These results show how well it works to combine math-based wavelet scattering features with regular machine learning models. This gives very good results while not needing large sets of data with labels.

8. CONCLUSION

This study presents a structured, resource-efficient framework for lung nodule detection, classification, and segmentation. This framework integrates the Wavelet Scattering Transform (WST) with traditional machine learning classifiers. The method achieves high performance without requiring large annotated datasets, making it well-suited for resource-limited clinical environments. WST ensures deformation stability and preserves critical high-frequency details, while the Support Vector Machine (SVM) emerged as the most effective classifier, achieving perfect accuracy across stratified 10-fold cross-validation. The lightweight Otsu-based segmentation pipeline demonstrated strong agreement with ground truth annotations, achieving a 0.912 on the dice and 0.845 on the IoU. Key contributions include a reproducible preprocessing pipeline—comprising denoising, intensity scaling, and gamma-based enhancement—optimized for CT imaging; robust and interpretable feature extraction using WST to distinguish benign from malignant nodules; comparative evaluation of SVM, RF, and DT classifiers, identifying SVM as optimal; and an efficient post-classification segmentation stage for accurate malignant nodule localization with minimal computational cost. These results highlight the framework's potential to improve early detection and care, which will ultimately lead to better patient outcomes. Despite its promising results, the study is limited by the use of a single dataset, and its performance may be affected by computational requirements and dataset-specific tuning, which suggest areas for future enhancement. Future work includes developing adaptive preprocessing, integrating advanced classification models, extending to 3D nodule analysis, and validating diverse datasets for enhanced generalizability.

Conflicts of Interest

The authors declare that they have no conflicts of interest.

Funding

None

Acknowledgment

None

References

[1] J. Ferlay, M. Ervik, F. Lam, M. Colombet, L. Mery, and M. Piñeros, *Global Cancer Observatory: Cancer Today*, International Agency for Research on Cancer (IARC) Working Group, Lyon, 2021. [Online]. Available: https://gco.iarc.fr/today

[2] A. Tiwari, "Prediction of lung cancer using image processing techniques: A review," *Advanced Computational Intelligence: An International Journal (ACII)*, vol. 3, no. 1, pp. 1–9, 2016. [Online]. Available: https://aircconline.com/acii/V3N1/3116acii01.pdf

[3] G. Silvestri, N. Tanner, P. Kearney, A. Vachani, P. Massion, A. Porter, S. Springmeyer, K. Fang, D. Midthun, and P. Mazzone, "Assessment of plasma proteomics biomarker's ability to distinguish benign from malignant lung nodules: Results of the PANOPTIC (Pulmonary Nodule Plasma Proteomic Classifier)," *Chest*, vol. 154, no. 3, pp. 491–500, 2018, doi: 10.1016/j.chest.2018.02.012.

[4] M. Nair, S. Sandhu, and A. Sharma, "Cancer molecular markers: A guide to cancer detection and management," *Semin. Cancer Biol.*, vol. 52, pp. 39–55, 2018, doi: 10.1016/j.semcancer.2018.02.002.

[5] S. Akila Agnes, A. Arun Solomon, and K. Karthick, "Wavelet U-Net++ for accurate lung nodule segmentation in CT scans: Improving early detection and diagnosis of lung cancer," *Biomed. Signal Process. Control*, vol. 87, no. 105509, 2024, doi: 10.1016/j.bspc.2023.105509.

[6] Abdollah Khorshidi, "Tumor segmentation via enhanced area growth algorithm for lung CT images," *BMC Med. Imaging*, vol. 23, no. 189, pp. 1–24, 2023, doi: 10.1186/s12880-023-01126-y.

[7] R. Liu, H. Nan, Y. Zou, T. Xie, and Z. Ye, "LSW-Net: A Learning Scattering Wavelet Network for Brain Tumor and Retinal Image Segmentation," *Electronics*, vol. 11, no. 16, pp. 1–14, 2022, doi: 10.3390/electronics11162616.

[8] E. H. Al-Saadi, A. N. Khdiar, and L. H. Al-Saadi, "An Automated Wavelet Scattering Network Classification Using Three Stages of Cataract Disease," *Baghdad Sci. J.*, vol. 21, no. 9, pp. 3044–3051, 2024, doi: 10.21123/bsj.2024.8995.

[9] H. Tianjiao, L. Yihua, Z. Yingqi, X. Jiashu, L. Shuai, and H. Chih-Cheng, "A lung nodule segmentation model based on the transformer with multiple thresholds and coordinate attention," *Sci. Rep.*, vol. 14, no. 31743, pp. 1–17, 2024, doi: 10.1038/s41598-024-82877-8.

[10] J. Feng and J. Jiang, "Deep learning-based chest CT image features in the diagnosis of lung cancer," *Comput. Math. Methods Med.*, vol. 2022, pp. 1–7, 2022, doi: 10.1155/2022/4153211.

[11] S. Zheng, L. Cornelissen, X. Cui, X. Jing, R. Veldhuis, M. Oudkerk, and P. Ooijen, "Deep convolutional neural networks for multiplanar lung nodule detection: Improvement in small nodule identification," *Med. Phys.*, vol. 48, pp. 733–744, 2021, doi: 10.1002/mp.14648.

[12] J. Soltani-Nabipour, A. Khorshidi, and B. Noorian, "Lung tumor segmentation using improved region growing algorithm," *Nucl. Eng. Technol.*, vol. 52, no. 10, pp. 2313–2319, 2020, doi: 10.1016/j.net.2020.03.011.

[13] M. Rehman, N. Nawi, A. Tanveer, H. Zafar, H. Munir, and S. Hassan, "Lung cancer nodules detection from CT scan images with convolutional neural networks," in *Proc. Int. Conf. Soft Comput. Data Mining*, 2020, pp. 382–391. doi: 10.1007/978-3-030-36056-6_36.

[14] R. Liu, H. Nan, Y. Zou, T. Xie, and Z. Ye, "LSW-Net: A Learning Scattering Wavelet Network for Brain Tumor and Retinal Image Segmentation," *Electronics (Basel)*, vol. 11, no. 2616, 2022, doi: 10.3390/electronics11162616.

[15] V. Khemani, M. H. Azarian, and M. G. Pecht, "Learnable Wavelet Scattering Networks: Applications to Fault Diagnosis of Analog Circuits and Rotating Machinery," *Electronics (Basel)*, vol. 11, no. 451, 2022, doi: 10.3390/electronics11030451.

[16] V. Bruni, M. L. Cardinali, and D. Vitulano, "An MDL-Based Wavelet Scattering Features Selection for Signal Classification," *Axioms*, vol. 11, no. 376, 2022, doi: 10.3390/axioms11080376.

[17] A. B. Buriro, B. Ahmed, G. Baloch, J. Ahmed, R. Shoorangiz, S. J. Weddell, and R. D. Jones, "Classification of alcoholic EEG signals using wavelet scattering transform-based features," *Comput. Biol. Med.*, vol. 139, no. 104969, 2021, doi: 10.1016/j.compbiomed.2021.104969.

[18] M. K. Yagnavajjula, K. R. Mittapalle, P. Alku, R. K. Sreenivasa, and P. Mitra, "Automatic classification of neurological voice disorders using wavelet scattering features," *Speech Commun.*, vol. 157, no. 103040, 2024, doi: 10.1016/j.specom.2024.103040.

[19] D. A. Pisner and D. M. Schnyer, *Support vector machine*, in *Machine Learning Methods and Applications to Brain Disorders*, Academic Press, pp. 101–121, 2020, doi: 10.1016/B978-0-12-815739-8.00006-7.

[20] A. Elhazmi, A. Al-Omari, H. Sallam, H. N. Mufti, A. A. Rabie, M. Alshahrani, A. Mady, A. Alghamdi, A. Altalaq, M. H. Azzam, A. Sindi, A. Kharaba, Z. A. Al-Aseri, G. A. Almekhlafi, W. Tashkandi, S. A. Alajmi, F. A. Faqihi, Alharthy, J. A. Al-Tawfiq, R. Ghazi Melibari, W. Al-Hazzani, and Y. M. Arabi, "Machine learning decision tree algorithm role for predicting mortality in critically ill adult COVID-19 patients admitted to the ICU," *J. Infect. Public Health*, vol. 15, pp. 826–834, 2022, doi: 10.1016/j.jiph.2022.06.008.

[21] I. Andyana, A. As-syakur, I. Sunarta, R. Suyarto, I. Diara, K. Susila, M. Saifulloh, T. Kusmiyarti, and W. Wiyanti, "Urban tourism expansion monitoring by remote sensing and random forest," in *Proc. 1st Int. Conf. Environmental Management (ICEM 2022)*, *IOP Conf. Ser. Earth Environ. Sci.*, vol. 1180, 012046, pp. 1–11, 2023, doi: 10.1088/1755-1315/1180/1/012046.

[22] Q. Song, L. Zhao, X. Luo, and X. Dou, "Using deep learning for classification of lung nodules on computed tomography images," *J. Healthcare Eng.*, vol. 2017, pp. 1–7, 2017, doi: 10.1155/2017/8314740.

[23] S. Hussein, R. Gillies, K. Cao, Q. Song, and U. Bagci, "TumorNet: lung nodule characterization using a multi-view convolutional neural network with Gaussian process," in *IEEE Int. Symp. Biomed. Imaging (ISBI)*, 2017, pp. 1–4. [Online]. Available: https://arxiv.org/abs/1703.00645

[24] Z. Nibali and D. Wollersheim, "Pulmonary nodule classification with deep residual networks," *Int. J. Comput. Assist. Radiol. Surg.*, vol. 12, pp. 1799–1808, 2017, doi: 10.1007/s11548-017-1605-6.

[25] W. Shen, M. Zhou, F. Yang, D. Yu, D. Dong, C. Yang, Y. Zang, and J. Tian, "Multi-crop convolutional neural networks for lung nodule malignancy suspiciousness classification," *Pattern Recognit.*, vol. 61, pp. 663–673, 2017, doi: 10.1016/j.patcog.2016.05.029.

[26] S. Hussein, K. Cao, Q. Song, and U. Bagci, "Risk stratification of lung nodules using 3D CNN-based multi-task learning," in *Information Processing in Medical Imaging*, vol. 10265, pp. 249–260, 2017, doi: 10.48550/arXiv.1704.08797.

[27] Y. Xie, Y. Xia, J. Zhan, D. Feng, M. Fulham, and W. Cai, "Transferable multi-model ensemble for benign-malignant lung nodule classification on chest CT," in *Lecture Notes in Comput. Sci.*, vol. 10435, pp. 656–664, 2017, doi: 10.1007/978-3-319-66179-7_75.

[28] Y. Xie, Y. Xia, J. Zhang, M. Fulham, and Y. Zhang, "Fusing texture, shape, and deep model-learned information at the decision level for automated classification of lung nodules on chest CT," *Inf. Fusion*, vol. 42, pp. 102–110, 2018, doi: 10.1016/j.inffus.2017.10.005.

[29] Y. Xie, Y. Xia, J. Zhang, Y. Song, D. Feng, M. Fulham, and W. Cai, "Knowledge-based collaborative deep learning for benign-malignant lung nodule classification on chest CT," *IEEE Trans. Med. Imaging*, vol. 38, no. 4, pp. 991–1004, 2019, doi: 10.1109/TMI.2018.2876510.

[30] G. Zhang, Z. Yang, L. Gong, S. Jiang, and L. Wang, "Classification of benign and malignant lung nodules from CT images based on hybrid features," *Phys. Med. Biol.*, vol. 64, no. 12, 2019, doi: 10.1088/1361-6560/ab2544.

[31] P. Wu, X. Sun, Z. Zhao, H. Wang, S. Pan, and B. Schuller, "Classification of lung nodules based on deep residual networks and migration learning," *Comput. Intell. Neurosci.*, vol. 2020, pp. 1–10, 2020, doi: 10.1155/2020/8975078.

[32] G. Shah, R. Thammasudjarit, A. Thakkinstian, and T. Suwatanapongched, "NoduleNet: a lung nodule classification using deep learning," *Ramathibodi Med. J.*, vol. 43, no. 4, pp. 11–19, 2020, doi: 10.33165/rmj.2020.43.4.241727.

[33] E. Lv, W. Liu, P. Wen, and X. Kang, "Classification of benign and malignant lung nodules based on deep convolutional network feature extraction," *J. Healthcare Eng.*, vol. 2021, no. 8769652, pp. 1–11, 2021, doi: 10.1155/2021/8769652.

[34] G. Zhang, L. Lin, and J. Wang, "Lung nodule classification in CT images using 3D DenseNet," *J. Phys.: Conf. Ser.*, vol. 1827, pp. 1–7, 2021, doi: 10.1088/1742-6596/1827/1/012155.

[35] P. Bruntha, S. Pandian, J. Anitha, S. Abraham, and S. Kumar, "A novel hybridized feature extraction approach for lung nodule classification based on transfer learning technique," *J. Med. Phys.*, vol. 47, no. 1, pp. 1–9, 2022, doi: 10.4103/jmp.jmp_61_21.